Experimental power balance study on turbulent heat transport at Wendelstein 7-X

OPEN ACCESS
IOP Publishing
Plasma Physics and Controlled Fusion
Plasma Phys. Control. Fusion **67** (2025) 075025 (12pp)
https://doi.org/10.1088/1361-6587/ade824

Experimental power balance study on turbulent heat transport at Wendelstein 7-X

M Wappl*, S A Bozhenkov, T Andreeva, S Bannmann, H M Smith, R C Wolf and the W7-X Team[1]

Max Planck Institute for Plasma Physics, Greifswald, Germany

E-mail: markus.wappl@ipp.mpg.de

Received 18 March 2025, revised 6 June 2025
Accepted for publication 25 June 2025
Published 7 July 2025

Abstract

Power balance analysis is used to compile an experimental database of turbulent heat transport in various plasma scenarios at the stellarator Wendelstein 7-X. As figures of merit for turbulence suppression, turbulent transport coefficients χ_e, χ_i and χ_{eff} are defined. The database spans a broad parameter range covering different fueling schemes, heating power values and sources as well as different magnetic configurations of W7-X. This paper seeks out correlations with main turbulence drivers to identify modes responsible for turbulent transport. ITG modes are thought to dominate the turbulent transport in W7-X. These modes are driven by a steep ion temperature gradient and suppressed by a density gradient, quantified by the parameters a/L_{Ti} and a/L_n (Beurskens *et al* 2021 *Nucl. Fusion* **61** 116072). Experiments with neutral beam or hydrogen pellet injection allow to increase the central density and thereby create steep density gradients. The database unveils a characteristic dependence of the turbulent transport coefficients on a/L_n and a/L_{Ti}, which is evidence for the prevalence of ITG modes. In plasmas with suppressed ITG modes, turbulent transport is reduced to near zero in the ion channel, but a residual level remains in the electron channel. Possible responsible modes are discussed. Global confinement time normalized to ISS04 is calculated independently from the power balance analysis, using diamagnetic loops and interferometry. It decays with increasing turbulent transport coefficients in the database and shows only minimal scatter. This serves as a cross-check for the power balance analysis. All plasmas achieving a normalized confinement time over one feature an increased density gradient. The modular coil system of W7-X opens up a wide space of magnetic configurations, including low and high magnetic mirror, low and high rotational transform ι as well as low shear. The configuration dependence of turbulent transport is discussed.

Keywords: EUROFUSION, WPW7X-PR, stellarator, power balance, turbulence

[1] See Grulke *et al* 2024 (https://doi.org/10.1088/1741-4326/ad2f4d) for the W7-X Team.

* Author to whom any correspondence should be addressed.

1. Introduction

The advanced stellarator Wendelstein 7-X is optimized with regards to minimized losses due to collisional transport of trapped particles, known as neoclassical transport. Substantially reduced neoclassical transport has been demonstrated in experiments [1]. As a consequence of the neoclassical optimization, the dominant remaining loss channel is turbulent transport, which is caused by a variety of different plasma instabilities. In the following, the most relevant instabilities for the W7-X experiment are briefly introduced, including ion temperature gradient modes (ITGs), electron temperature gradient modes (ETG), trapped electron modes (TEM) and kinetic ballooning modes (KBM).

ITG, ETG and TEM are classified as drift wave instabilities. Configurations of W7-X appear quite prone to ITG driven instabilities. These modes become destabilized above a critical boundary of the inversed T_i gradient length ($a/L_{T\mathrm{i}}$) [2–5],

$$a/L_{T\mathrm{i}} = -\frac{a}{T_\mathrm{i}}\frac{\mathrm{d}T_\mathrm{i}}{\mathrm{d}r_\mathrm{eff}}. \tag{1}$$

The density gradient driven drift wave mechanism competes with ITG growth [5]. Hence, the strongest mechanism to suppress ITG modes is a pronounced electron density gradient, quantified by the parameter a/L_n, which offers a path to improved confinement,

$$a/L_n = -\frac{a}{n}\frac{\mathrm{d}n}{\mathrm{d}r_\mathrm{eff}}. \tag{2}$$

A common criterion for ITG stability is linked to the parameter η, which has to be below a certain critical value [2],

$$\eta = \frac{\mathrm{d}(\ln T_\mathrm{i})}{\mathrm{d}(\ln n)}. \tag{3}$$

In W7-X, ITG modes are partially responsible for the so-called ion temperature clamping, which limits the central ion temperature to approximately 1.5 keV in a wide range of scenarios. ITG turbulence is further exacerbated by the ratio of $T_\mathrm{e}/T_\mathrm{i}$, which enhances ion turbulent transport especially in ECR heated plasmas [6].

In addition, the ambipolar electric field can play a secondary role to ITG suppression via the induced $E \times B$-shear [7, 8]. Strong electric field shear in the edge pedestal of tokamaks leads to turbulence suppression responsible for the H-mode.In stellarators, large electric field gradient and $E \times B$ shear could be reached near to the transition from electron root to ion root and mitigate turbulence [9], however has yet to be demonstrated experimentally.

ITG modes are on the spatial scale of the ion gyroradius, therefore ITG-driven turbulent transport is expected to scale with the magnetic field and temperature like the ion gyroradius, known as gyro-Bohm scaling [10]. The effect of ITG modes on turbulent transport in W7-X has been modeled in gyrokinetic simulations [11]. Non-linear GK simulations show a very clear reduction of turbulent transport in with density gradient in W7-X, which is in contrast to other stellarator configurations [12]. First-principle profile predictions find that ion temperature clamping in W7-X is primarily due to inefficient thermal electron-ion coupling in a turbulence-dominated regime, while at high $T_\mathrm{e}/T_\mathrm{i}$ the clamping is exacerbated by turbulence stiffness connected to ion-scale turbulence [13].

ETGs are driven by a mechanism analogous to ITGs, being destabilized by the ETG and stabilized by the density gradient [5],

$$a/L_{T\mathrm{e}} = -\frac{a}{T_\mathrm{i}}\frac{\mathrm{d}T_\mathrm{e}}{\mathrm{d}r_\mathrm{eff}}. \tag{4}$$

They are on the scale of the electron gyroradius, leading to the expectation that ETG-driven turbulent transport is several orders of magnitude smaller than for ITGs [3]. However, the formation of elongated vortices called streamers can lead to very effective transport [14]. It is found in simulations that they may cause ion scale turbulence in the electron channel, that can dominate turbulent transport in improved performance scenarios [15].

TEMs can be driven by density gradients or ETGs and rely on particles trapped in a magnetic well. W7-X is stable against the density gradient driven type [5, 16]. TEMs can cause heat transport in both the electron and ion channel [3]. Gyrokinetic studies show a dominant role of density gradient driven TEMs in the optimized quasi-helically symmetric stellarator HSX [17] and a geometry-dependent TEM stabilization at high collisionality in DIII-D, HSX and W7-X [18].

At low collisionalities, TEM combined with ITG modes account for the turbulent transport in W7-X. Doppler reflectometry shows reduced core fluctuations in low collisionality plasmas, while turbulent transport is unchanged. This is likely due to a shift from ITG mode to TEM activity, which is not picked up by Doppler reflectometry due to the different toroidal location [19, 20].

In this paper, the measure for collisionality is the normalized collisionality ν^*, with the major radius R, rotational transform ι, electron thermal velocity v_e and the collision frequency ν [21],

$$\nu^* = \frac{R\,\nu}{\iota\, v_\mathrm{e}} \sim \frac{n_\mathrm{e}}{T_\mathrm{e}^2}. \tag{5}$$

It is proportional to the electron density n_e and the inverse electron temperature T_e squared.

The aforementioned instabilities stem from electrostatic effects. In contrast, ballooning modes are fundamental MHD instabilities in toroidal geometry, caused by the product of the magnetic field curvature and the pressure gradient [22]. Including kinetic effects leads to the theory of KBMs [23]. KBMs exhibit a sharp threshold in plasma β above which they become destabilized [4]. At high plasma pressure, ITG and TEM may be suppressed due to finite-β effects and KBMs may become responsible for turbulent transport [24].

Turbulent transport driven by gyroradius-scale instabilities without long-range coupling is expected to scale according to the gyro-Bohm scaling [25]. It follows from a random walk assumption, where the step size is the gyroradius and the step

frequency is the drift frequency [3]. Gyro-Bohm like temperature scaling has been confirmed in discharges with reduced turbulence at W7-X [26]. Heat fluxes and transport coefficients in both experiment and theory are commonly normalized to the associated heat flux q_{gB} and transport coefficient χ_{gB},

$$q_{\mathrm{gB}} = n\,T\frac{r_{\mathrm{L}}^2\,c_{\mathrm{s}}}{a^2} \sim \frac{n\,T^{5/2}}{a^2\,B^2} \tag{6}$$

$$\chi_{\mathrm{gB}} = \frac{r_{\mathrm{L}}^2\,c_{\mathrm{s}}}{a} \sim \frac{T^{3/2}}{a\,B^2}. \tag{7}$$

The magnetic configuration space of W7-X offers several degrees of freedom. This work considers the magnetic mirror ratio ϵ_{eff} and the rotational transform ι, which can be varied to a low- and high mirror configuration, several low- and high ι configurations [27] as well as a low shear configuration. The configuration in the middle of this parameter space is called the standard configuration. Some intermediate configurations between standard and high ι behave as limiter configurations with internal magnetic islands. These are proven to have improved global confinement compared to the standard configuration [27].

Turbulent transport and its driving instabilities have been in the focus of magnetic confinement fusion research for several decades. They can be studied by an array of different experimental methods.

Firstly, power balance analysis involves balancing all known energy sources and sinks against the heat flux in a plasma, such that energy continuity is fulfilled. It requires high-quality plasma profiles as well as modeling of the heating sources, calculation of neoclassical losses and subtraction of radiated power, while unaccounted losses are attributed to turbulent transport. This allows to extract turbulent heat fluxes and turbulent transport coefficients. Multiple studies have applied power balance analysis to W7-X before [20, 28], also in direct comparison to the Heliotron LHD [29]. Major findings are that ITG modes are a prominent instability in both devices, with neoclassical transport being dominant in LHD and turbulent transport dominating in W7-X. There have been more power balance studies focused on the stellarators Heliotron-J [30–32] and HSX [33], for both of which significant turbulent transport is found. Furthermore, the same approach is also known from tokamak experiments including DIII-D [34], which also identified ITG modes as a turbulence driver [35], JET [36], which included the time derivative of the thermal stored energy [37] as well as ASDEX Upgrade [38, 39], EAST [40], JT-60 [41, 42] and KSTAR [43].

Another method to determine turbulent transport coefficients is heat pulse propagation. Electron heat pulse studies utilize a modulation of microwave heating power to modify the local ETG. An electron temperature diagnostic with sufficient time resolution like the electron cyclotron emission (ECE) diagnostic measures the evolution of T_{e}. Solving the heat transport equation yields electron transport coefficients [44]. A study at LHD has compared turbulent transport coefficients obtained by ECRH modulation and power balance analysis, with good agreement [45].

Similarly, ion heat transport can be determined by observing ion temperature fluctuations in neutral beam experiments. This has been reported in conferences [46, 47] and suitable high-speed spectrometers were recently installed at W7-X [26].

Plasma turbulence is accompanied by density fluctuations, which can be measured with a reflectometer [20] and other methods such as phase contrast imaging (PCI) [48]. Doppler reflectometry has been used in a study on turbulence in different W7-X scenarios on the basis of density fluctuations. In a similar fashion to this paper, it has sought correlations of density fluctuations with the parameters a/L_n, $a/L_{T\mathrm{i}}$, $a/L_{T\mathrm{e}}$, $T\mathrm{e}/T\mathrm{i}$, E_{r} and ν [19].

In addition to measurements of turbulent heat transport, there are methods to evaluate turbulent particle and impurity transport. Similar to power balance analysis, turbulent particle transport can be inferred from the particle continuity equation [49]. The active charge exchange recombination spectroscopy (CXRS) diagnostic can determine diffusion and convection coefficients of one-dimensional impurity transport with help of the pySTRAHL code [50]. Impurity transport can furthermore be monitored with the concentration of tracer ions introduced by the laser blow-off (LBO) technique [51, 52].

This paper sets out to create an extensive experimental database of turbulent transport coefficients in various plasma scenarios at Wendelstein 7-X, obtained from power balance analysis. It covers different fueling schemes, heating power values and methods as well as different magnetic configurations and seeks out correlations with main turbulence drivers to identify modes responsible for turbulent transport. Central densities range from $2\times10^{19}\,\mathrm{m}^{-3}$ to $2\times10^{20}\,\mathrm{m}^{-3}$ with ECR heating power between 500 kW and 7 MW. The analysis supports the dominant role of ITG turbulence for heat transport in W7-X.

The paper is organized as follows. In the second chapter, details and caveats of the power balance analysis used for the database are laid out. Plasma scenarios of suppressed turbulent heat transport are discussed in detail in the third chapter. Correlations in the experimental database are discussed in the fourth chapter. The findings are concluded in the fifth chapter.

2. Methodology

Power balance analysis requires high-quality plasma profiles and information on heating sources. For the analysis presented in this work, electron density and temperature data are acquired by the Thomson scattering diagnostic [53–55]. Ion temperatures are taken from the x-ray imaging crystal spectroscopy (XICS) or CXRS diagnostics.

XICS relies on diagnostic injection of Argon gas to measure the Doppler broadening of characteristic x-rays from Ar16+. Tomographic inversion of multiple line integrated measurements generates temperature profiles [56, 57]. There appears to be an offset of 0–300 eV in ion temperatures measured with XICS. Near the plasma edge T_{i} must be equilibrated to T_{e}, otherwise unphysically large collisional heat exchange

occurs [58]. The offset in XICS is corrected to match the electron temperature in the outer half radius as well as CXRS, if available [59].

Active CXRS is based on charge exchange between injected neutral particles and the intrinsic impurity carbon. The process leaves carbon ions in an excited state with subsequent emission of characteristic light in the visible range. From Doppler broadening of this emission, CXRS measures ion temperatures in localized measurement volumes and allows to construct profiles.

Because of the well established spectral measurement techniques in the visible range and the local nature of the measurements, CXRS often provides more accurate profiles than XICS. However, CXRS is only available in discharges with neutral beam injection (NBI) or diagnostic neutral beam blips [59, 60]. Ion temperature profile fits are produced from CXRS, XICS or the combination of both diagnostics, based on availability.

There are two substantial heating systems in use at W7-X: electron cyclotron resonance heating (ECRH) and NBI.

The ECRH beam has a Gaussian power density profile [61]. For the power balance analysis, ECRH power is taken from machine parameters and microwave absorption is approximated by a Gaussian in r_{eff}, centered on the magnetic axis [58]. In the presented database plots, the ECRH absorption zone is excluded. A more precise microwave power deposition profile can be attained with a ray tracing code such as TRAVIS [28].

Fast ion birth profiles due to NBI heating are calculated with a beam model that solves a collisional-radiative model using Bayesian inference from beam emission spectroscopy. Acceleration voltage, current and intensity fraction of each energy component of the neutral beam are deduced from the neutralizer spectroscopy [58]. From the fast ion birth rates of each energy component, power fractions deposited to electrons and ions are obtained by analytical slowing-down calculation [62]. The beam model neglects fast ion drifts and losses. In a validation against BEAMS3D [63], the beam model found 12% higher power for electrons and 19% higher power for ions [58].

A Bolometer system measures power losses due to plasma radiation. The radiation profile needed for power balance analysis is obtained from tomographic inversion [64, 65].

Two web-applications facilitate the data analysis. The density and temperature profiles are mapped to a magnetic equilibrium reconstruction from the variational moments equilibrium code (VMEC) [66] and fitted as functions of effective minor radius with the web-app Profile Cooker [58]. Monte–Carlo sampling allows propagation of the fit uncertainties in the power balance analysis. Solving the power balance equation and organizing the results into a database is handled by the web-app Power House [58].

Neoclassical transport needs to be subtracted from the power balance in order to isolate the turbulent transport. In general stellarators, a radial electric field arises to balance the neoclassical fluxes of positive and negative charges to fulfill the condition of ambipolarity. This may yield an ion root and an electron root solution [67]. Within the web-app Power House, neoclassical particle and heat fluxes alongside the ambipolar electric field are computed with the neoclassical code Neotransp [1, 68] by integrating mono-energetic transport coefficients obtained from the drift kinetic equation solver (DKES) [66, 69] over a Maxwellian distribution.

In the presence of both root solutions, Neotransp models the electric field by a thermodynamic approach minimizing the total heat production from rotation shear and neoclassical transport, which has the form of a diffusion equation (8) [67],

$$\frac{\partial E_{\mathrm{r}}}{\partial t} - \frac{1}{V'}\frac{\partial}{\partial r_{\mathrm{eff}}} D_E\, V'\, r_{\mathrm{eff}} \frac{\partial}{\partial r_{\mathrm{eff}}}\frac{E_{\mathrm{r}}}{r_{\mathrm{eff}}} = \frac{|e|}{\epsilon}\left(\Gamma_{\mathrm{NC},e} - Z_{\mathrm{i}}\,\Gamma_{\mathrm{NC,i}}\right). \tag{8}$$

The free parameter D_E controls the width of the root transition area. Electric fields obtained with DKES were validated against other neoclassical codes and measurements by the diagnostic XICS at W7-X [70], as well as compared to CXRS measurements [71]. A global, self-consistent simulation [72] with the gyrokinetic code EUTERPE [73] found good agreement with Neotransp for the electric field root solutions, while in the root transition region the gradient of E_{r} could be reproduced by equation (8) for suitable D_E [58].

For the heat fluxes in the power balance analysis in this study, the electron root solution is used where the obtained electric field is positive and the ion root solution where the electric field is negative.

Centerpiece of the analysis is the power balance equation, which derives from an energy continuity equation,

$$\frac{\partial E_{\mathrm{kin}}}{\partial t} = -\left(q_{\mathrm{NC}} + q_{\mathrm{turb}}\right) V' + P_{\mathrm{heat}} + P_{\mathrm{exchange}} - P_{\mathrm{rad}}. \tag{9}$$

P_{heat} is determined for ECRH and NBI as described above, P_{rad} by Bolometer, while $\frac{\partial E_{\mathrm{kin}}}{\partial t}$ and P_{exchange} are calculated from kinetic profiles. q_{NC} is calculated by Neotransp and V' comes from the VMEC equilibrium. Once all other contributions to the power balance are ascertained, the turbulent heat flux q_{turb} can be extracted. The radially resolved power balance equation is solved for electrons, ions and the single fluid plasma.

A diffusive model is chosen for turbulent transport, which is in line with other experimental works [6, 26, 29]. From turbulent fluxes, turbulent transport coefficients are defined,

$$\chi_{\mathrm{e}} = -\frac{q_{\mathrm{turb,e}}}{n_{\mathrm{e}}\, T'_{\mathrm{e}}} \tag{10}$$

$$\chi_{\mathrm{i}} = -\frac{q_{\mathrm{turb,i}}}{n_{\mathrm{i}}\, T'_{\mathrm{i}}} \tag{11}$$

$$\chi_{\mathrm{eff}} = -\frac{q_{\mathrm{turb}}}{n_{\mathrm{e}} T'_{\mathrm{e}} + n_{\mathrm{i}}\, T'_{\mathrm{i}}}. \tag{12}$$

These transport coefficients serve as figures of merit for turbulent transport in a given plasma scenario, so they can be compared for relevant plasma parameters and magnetic configurations in the database. Heat fluxes as well as turbulent transport coefficients are to be understood as flux surface averaged [58].

Table 1. Numbers of data points with available χ_{eff}, itemized by heating and fueling scheme as well as magnetic configuration.

	Pure ECRH	Pure NBI	ECRH+NBI	ECRH+pellets	
Standard	58	3	17	58	136
High mirror	42	12	13	6	73
Low mirror	8	3	21	2	34
High ι	85	2	5	14	106
Low ι	26	0	2	1	29
Low shear	7	0	2	0	9
	226	20	60	81	387

Table 2. Numbers of data points with available χ_{e} and χ_{i}, itemized by heating and fueling scheme as well as magnetic configuration.

	Pure ECRH	Pure NBI	ECRH+NBI	ECRH+pellets	
Standard	49	0	15	49	113
High mirror	38	0	12	5	55
Low mirror	8	0	20	2	30
High ι	75	0	3	13	91
Low ι	22	0	2	1	25
Low shear	7	0	0	0	7
	199	0	52	70	321

To avoid problems with vanishing profile gradients and highly localized power deposition near the magnetic axis, as well as interaction with neutral gas and PFCs, determination of transport coefficients is generally limited to the range of 0.1 m $\leqslant r_{\mathrm{eff}} \leqslant$ 0.4 m [58]. By comparison, the effective minor radius of W7-X extends to roughly $r_{\mathrm{eff}} = 0.5$ m and depends on the magnetic configuration.

At radial positions where electron and ion temperatures are too close together to separate due to diagnostic accuracy, they are assumed to be equilibrated, since a small difference in a large volume near the plasma edge would lead to an unphysically large collisional heat exchange term P_{exchange} [58]. In many cases with direct ion heating through NBI, density is high while electron and ion temperatures are close together even on the magnetic axis. This leads to large uncertainty in the collisional heat exchange term P_{exchange}, so that χe and χi cannot be disentangled [59]. For such cases, only the effective turbulent transport coefficient χ_{eff} can be measured.

The presented database contains discharges from 2018 to 2025, corresponding to the operation phases OP1.2b, OP2.1., OP2.2 and OP2.3. Analysis of further discharges from OP2.2 and OP2.3 is still ongoing. It includes hydrogen discharges fueled by gas inlet as well as neutral beam and pellet injection. Heating is provided by ECRH, NBI or combinations of both. In total, the database comprises 387 data points representing different time points from 175 W7-X discharges. In a reduced database eliminating cases where χ_{e} and χ_{i} cannot be separated and only χ_{eff} is available, 321 data points from 156 discharges remain. Tables 1 and 2 hold the numbers of data points itemized by heating and fueling scheme as well as magnetic configuration, for the total database with available χ_{eff} in table 1 and for the reduced database with available $\chi_{\mathrm{e}}/\chi_{\mathrm{i}}$in table 2.

3. Experimental data and plasma scenarios

In order to illustrate different plasma scenarios found in the database, this section presents three discharges in detailed plots. This includes the density and temperature profiles, the corresponding inverse gradient lengths, ambipolar electric field and field gradient as well as the turbulent transport coefficients obtained by power balance analysis. The latter are also compared to the gyro-Bohm scaled transport coefficients χ_{gB}. Raw profile data are omitted for clarity, the fits of density and temperature with uncertainties based on Monte–Carlo sampling were created in the web-app Profile Cooker [58]. The radial range of the profiles extends from the magnetic axis to the LCFS of W7-X, $r_{\mathrm{eff}} \approx$ 0.5 m. Reliable power balance analysis is possible within 0.1 m $\leqslant r_{\mathrm{eff}} \leq$ 0.4 m [58].

Figure 1 shows W7X20180920.013, a 4.7 MW ECR-heated and gas fueled discharge in standard configuration (EJM001+252). This case serves as a benchmark without turbulence suppression that has a long, stationary averaging time window, which is favorable for profile quality. The density profile is largely flat with a/L_n smaller than $a/L_{T\mathrm{i}}$ throughout the radius and the ion temperature is in the typical clamping limit. Neotransp finds an ambipolar electric field purely in ion root, with small values within $\pm 10\,\mathrm{kVm}^{-1}$ and a small field gradient. Turbulent transport appears to be dominated by the ion channel, χ_{i} is in the same order of magnitude as the gyro-Bohm scaling coefficient and χ_{e} is smaller at $\approx 0.5\,\mathrm{m}^2\mathrm{s}^{-1}$.

Figure 2 shows the 4.6 MW ECR-heated, pellet fueled, standard configuration (EJM001+252) case W7X20181016.037. In such discharges a series of hydrogen pellets is injected to raise the core density. The time point of the analysis is chosen at the peak performance, which is

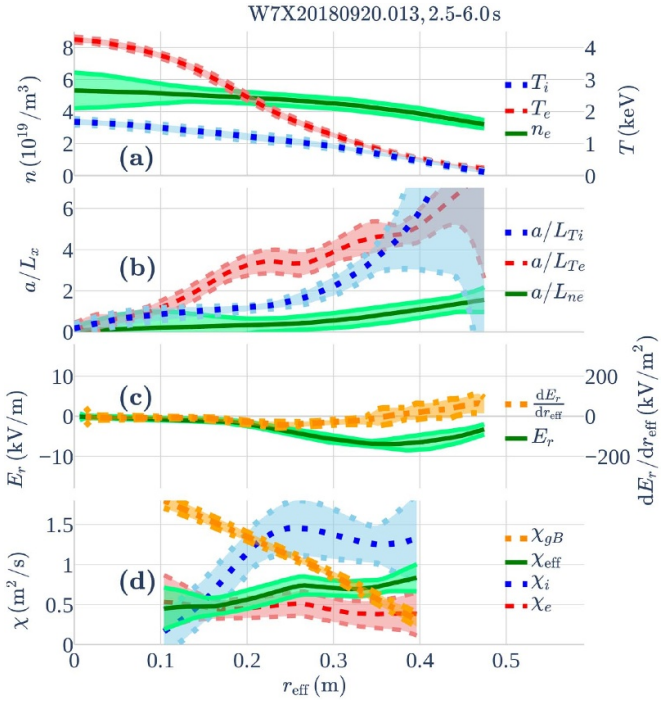

Figure 1. Power balance analysis of W7X20180920.013. Standard configuration (EJM001+252). Color bands represent uncertainties of $\pm 3\,\sigma$. (a) Electron/ion density (green, solid line), electron temperature (red, dashed line) and ion temperature (blue, dotted line). (b) Inversed gradient lengths of electron/ion density (green, solid line), electron temperature (red, dashed line) and ion temperature (blue, dotted line). (c) Ambipolar electric field (green, solid line) and electric field gradient (orange, dashed-dotted line). (d) Turbulent transport coefficients of electrons (red, dashed line), ions (blue, dotted line) and effective (green, solid line) compared to gyro-Bohm scaling (orange, dashed-dotted line).

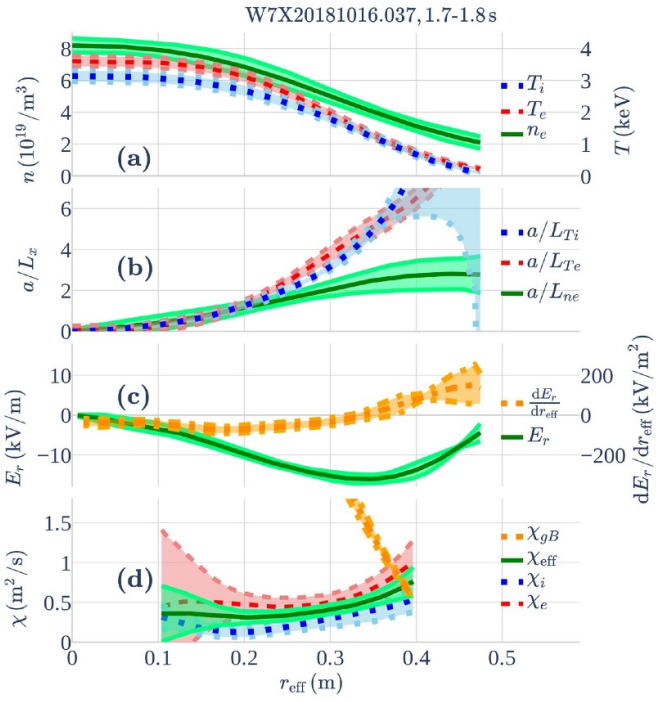

Figure 2. Power balance analysis of W7X20181016.037. Standard configuration (EJM001+252). For color coding see figure 1.

reached transiently after the pellet injection phase [28].This plasma is characterized by a large core density with a steep density gradient and increased a/L_n. Ion temperature clamping is overcome in this shot at $T_\mathrm{i} \approx 3\,\mathrm{keV}$. The electric field is strongly negative (ion root), however with only a small gradient. Turbulent transport in the ion channel is suppressed to almost zero, which can be attributed to the effect of the density gradient. The electron transport is less affected by the density gradient and remains at the same level of $\approx 0.5\,\mathrm{m^2 s^{-1}}$ as in W7X20180920.013. Due to the higher ion temperature, the gyro-Bohm scaling coefficient is increased compared to W7X20180920.013 and is an order of magnitude greater than χ_{eff} at mid radius.

During post-pellet phases in W7-X, a reduced amplitude of density fluctuations indicating turbulence suppression is found with Doppler reflectometry [74]. A pellet-induced improvement of confinement and central ion temperature has also been reported from the stellarator TJ-II [75].

The third detailed discharge is W7X20221123.003 in figure 3, which is a stationary low-power 1.5 MW ECR-heated, gas fueled case, following a boronization of the first wall. The magnetic configuration is high ι (FTM001+2512), which does not have internal islands [27]. This case features much smaller central electron density with a/L_n also small in the center, but a spontaneous density gradient develops in the radial range of $r_{\mathrm{eff}} > 0.2\,\mathrm{m}$, which significantly improves plasma performance. Such plasmas scenarios can be maintained for multiple seconds. Once again, this discharge overcomes the typical ion temperature clamping limit and reaches $T_\mathrm{i} \approx 2\,\mathrm{keV}$. The electric field near the center is in electron root and transitions to ion root between $r_{\mathrm{eff}} = 0.15$ to $0.2\,\mathrm{m}$. In the transition area, a strong, negative electric field gradient is found. There is clear turbulence suppression both for both electrons and ions, which is near complete for the ions in the area of the root transition and χ_{gB} is again far greater than the found turbulent transport coefficients. Note that the neoclassical transport is overestimated near to the root transition due to the underlying drift kinetic approximation [58], which leads to underestimated turbulent transport. However, this does not affect the measurements at other radial positions.

First wall coating improves density control because it reduces hydrogen outgassing. This has also been reported for TJ-II before, in that case yielding better results with lithium than boron [76].

In both the pellet fueled and post boronization cases, the inverse density gradient length is above unity in a wide range. This allows for ITG suppression and explains the reduced turbulent transport coefficient especially in the ion channel. In contrast, W7X20180920.013 exhibits smaller a/L_n and subsequently larger transport coefficients.

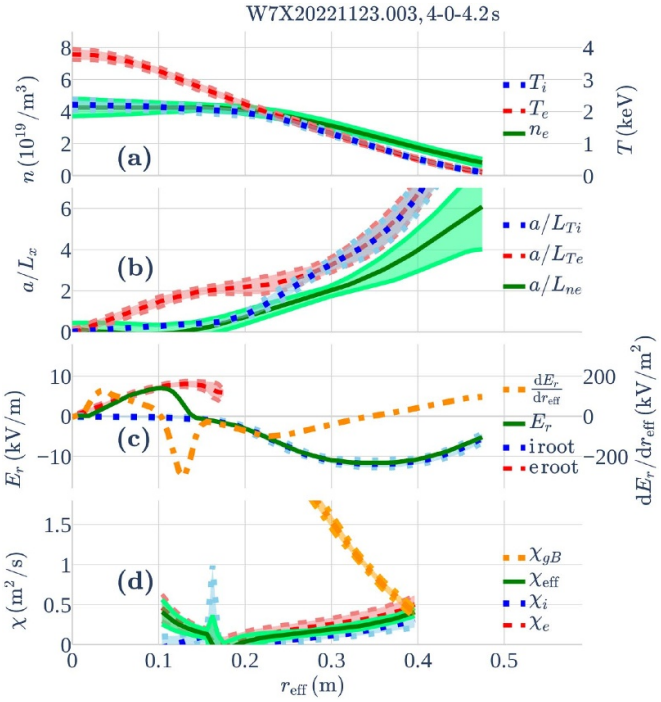

Figure 3. Power balance analysis of W7X20221123.003. High ι configuration (FTM001+2512). For color coding see figure 1. Added in (c) electron root (red, dashed line), ion root (blue, dotted line).

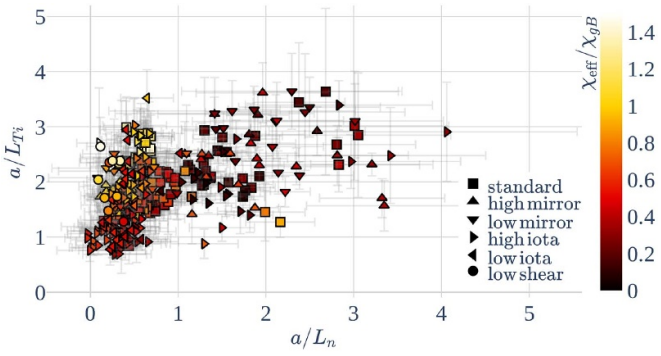

Figure 4. Scatterplot of gyro-Bohm normalized effective turbulent transport coefficient $\chi_{\mathrm{eff}}/\chi_{\mathrm{gB}}$ color-scaled over inverse density gradient length a/L_n and inverse ion temperature gradient length a/L_{Ti}. Error bars represent uncertainties of $\pm 3\,\sigma$, $r_{\mathrm{eff}} = 0.25$ m.

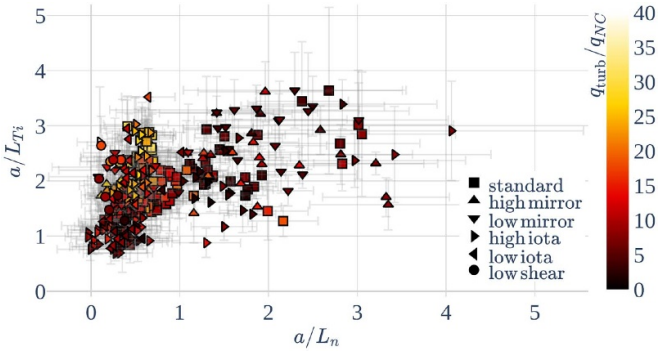

Figure 5. Scatterplot of turbulent- divided by neoclassical heat flux $q_{\mathrm{turb}}/q_{\mathrm{NC}}$ color-scaled over inverse density gradient length a/L_n and inverse ion temperature gradient length a/L_{Ti}. Error bars represent uncertainties of $\pm 3\,\sigma$, $r_{\mathrm{eff}} = 0.25$ m.

4. Database results

This section summarizes dependencies of the turbulent transport coefficients on physical parameters in overview plots. The plots contain data points, each of which represents a time point of a discharge in the power balance database. χ_{e}, χ_{i} and χ_{eff} in all plots are turbulent transport coefficients with neoclassical transport subtracted. All data points are evaluated at $r_{\mathrm{eff}} = 0.25$ m, which is roughly half of the minor radius of W7-X and allows for accurate power balance analysis and meaningful comparison of plasma scenarios. Magnetic configurations are indicated by the symbols in all the plots, error bars correspond to three times the standard deviation ($\pm 3\,\sigma$).

To give an overview of turbulence suppression with density and ion temperature gradient lengths, figure 4 shows a scatterplot of a/L_n and a/L_{Ti} with $\chi_{\mathrm{eff}}/\chi_{\mathrm{gB}}$ color-scaled.

Figure 5 compares the turbulent heat flux q_{turb} to the neoclassical heat flux q_{NC}.

Data points with relatively small turbulent transport seem to aggregate in the area of $a/L_{Ti} < 1.5$ and small a/L_n, while the lowest $\chi_{\mathrm{eff}}/\chi_{\mathrm{gB}}$ are exclusively found at $a/L_n > 1$. Doppler reflectometry yields similar trends of the density fluctuation amplitude with a/L_{Ti} and a/L_n [19].

Turbulent transport found in the database typically exceeds neoclassical transport by more than a factor of 10, only some turbulence suppressed scenarios with $a/L_{Ti} < 1.5$ and small $a/L_n > 1$ form an exception, as seen in figure 5.

Since the dependencies on a/L_{Ti} and a/L_n are fundamentally important, they are also illustrated by slicing and projecting the plot in figure 4 to the corresponding axis. Figure 6 shows $\chi_{\mathrm{eff}}/\chi_{\mathrm{gB}}$ over the inverse density gradient length a/L_n for the data points with $a/L_{Ti} > 1.5$, where there is sufficient coverage with data points across the full range of a/L_n. A reduction in turbulent transport with inverse density gradient length is clearly apparent. There seem to be two distinct transport regimes. $\chi_{\mathrm{eff}}/\chi_{\mathrm{gB}}$ is roughly inversely proportional to a/L_n for $a/L_n < 1$. For $a/L_n > 1$, $\chi_{\mathrm{eff}}/\chi_{\mathrm{gB}}$ is low and nearly constant. In this region, ITG modes are likely stabilized and the remaining turbulent transport is due to another microinstability not correlated to the density gradient. This is further illustrated with separated plots for the electron and ion channel in figure 13 and 14 below.

Between $a/L_n = 1$ and 2, there are some outliers in the high mirror configuration, for which the reduction in turbulent transport is less effective. A strong reduction in turbulent is only reached above $a/L_n = 2$ in the high mirror configuration.

Conversely, figure 7 plots $\chi_{\mathrm{eff}}/\chi_{\mathrm{gB}}$ over the inverse ion temperature gradient length a/L_{Ti} for all data with $a/L_n < 1$, where the largest range of a/L_{Ti} is covered. Figure 7 shows a trend to higher $\chi_{\mathrm{eff}}/\chi_{\mathrm{gB}}$ at larger a/L_{Ti}, with values over one

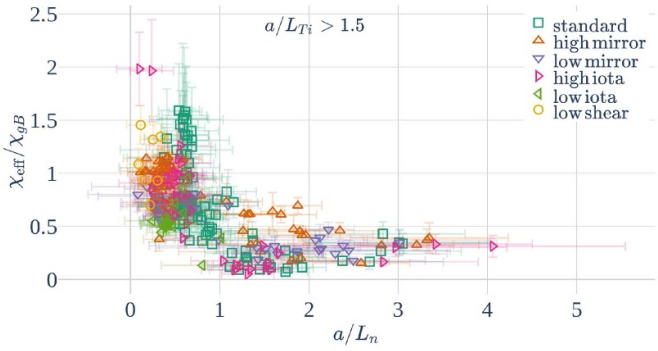

Figure 6. Scatterplot of gyro-Bohm normalized effective turbulent transport coefficient $\chi_{\mathrm{eff}}/\chi_{\mathrm{gB}}$ over inverse density gradient length a/L_n, data points are limited to $a/L_{Ti} > 1.5$. Error bars represent uncertainties of $\pm 3\,\sigma$, $r_{\mathrm{eff}} = 0.25$ m.

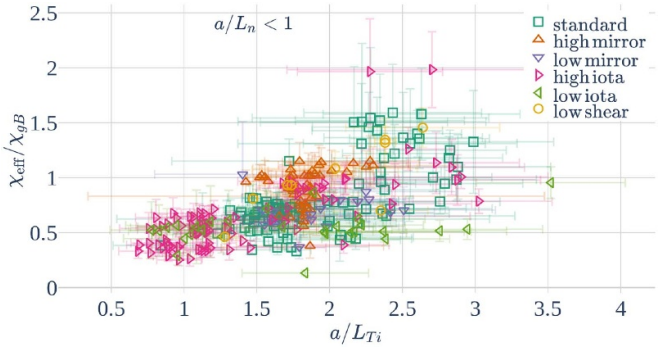

Figure 7. Scatterplot of gyro-Bohm normalized effective turbulent transport coefficient $\chi_{\mathrm{eff}}/\chi_{\mathrm{gB}}$ over inverse ion temperature gradient length a/L_{Ti}, data points are limited to $a/L_n < 1$. Error bars represent uncertainties of $\pm 3\,\sigma$, $r_{\mathrm{eff}} = 0.25$ m.

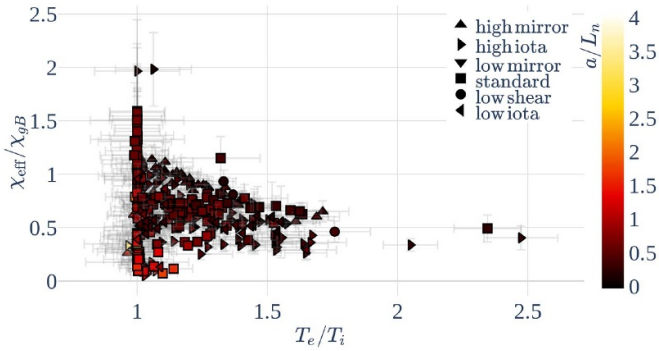

Figure 8. Scatterplot of gyro-Bohm normalized effective turbulent transport coefficient $\chi_{\mathrm{eff}}/\chi_{\mathrm{gB}}$ over temperature ratio T_e/T_i, a/Ln as color-scale. Error bars represent uncertainties of $\pm 3\,\sigma$, $r_{\mathrm{eff}} = 0.25$ m.

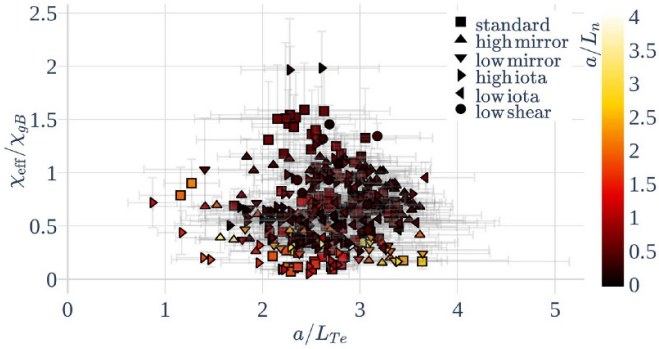

Figure 9. Scatterplot of gyro-Bohm normalized effective turbulent transport coefficient $\chi_{\mathrm{eff}}/\chi_{\mathrm{gB}}$ over inverse electron temperature gradient length a/L_{Te}, a/Ln as color-scale. Error bars represent uncertainties of $\pm 3\,\sigma$, $r_{\mathrm{eff}} = 0.25$ m.

appearing at $a/L_{Ti} > 1.5$. However, there seems to be no critical change in transport regime, as well as no turbulence suppression as strong as with a/L_n. The values of a/L_{Ti} appear more widely scattered than for a/L_n, which could be caused by off-axis NBI heating in some discharges or the comparatively weak profile stiffness in W7-X.

To further investigate correlations in the large cloud of data points which are not subject to strong turbulence suppression, the following figures are color-scaled for a/L_n.

Figure 8 shows the dependence of $\chi_{\mathrm{eff}}/\chi_{\mathrm{gB}}$ on the temperature ratio $T_{\mathrm{e}}/T_{\mathrm{i}}$. At low $T_{\mathrm{e}}/T_{\mathrm{i}}$ ratio, there is a wide distribution of $\chi_{\mathrm{eff}}/\chi_{\mathrm{gB}}$ values, while for a large ratio $\chi_{\mathrm{eff}}/\chi_{\mathrm{gB}}$ seems to converge to a value near 0.6. No clear exacerbation of turbulent transport with increasing $T_{\mathrm{e}}/T_{\mathrm{i}}$ can be seen in the database. A possible dependence of $T_{\mathrm{e}}/T_{\mathrm{i}}$ is likely masked by stronger parameter dependencies like that with the temperature gradient. Therefore, to measure the $T_{\mathrm{e}}/T_{\mathrm{i}}$ effect, a carefully conducted set of experiments with well controlled profile gradients would be necessary. Yet, this effect does not seem to be dominant in the database.

There are no data in the space of $T_{\mathrm{e}}/T_{\mathrm{i}} < 1$, which is inaccessible with the heating capabilities of W7-X. Doppler reflectometry also finds no clear trend of density fluctuations with $T_{\mathrm{e}}/T_{\mathrm{i}}$ [19].

Figure 9 contains a plot of $\chi_{\mathrm{eff}}/\chi_{\mathrm{gB}}$ over the inverse ETG length a/L_{Te}.

No turbulence suppression with a/L_{Te} can be observed. However, the presence of ETG modes cannot be excluded based on this, since the range of a/L_{Te} is much smaller than that covered by a/L_{Ti}, with few data points at $a/L_{Te} < 2$.

In figure 10, $\chi_{\mathrm{eff}}/\chi_{\mathrm{gB}}$ is plotted over the normalized collisionality ν^*. There is a recognizable trend to increasing turbulent transport at the highest collisionality values. This is in contrast to the expected behaviour for TEMs, which are thought to be suppressed at high collisionality, and also to the experimental finding that TEMs combined with ITG modes lead to transport unchanged by collisionality [20]. This disagreement alone does not necessarily exclude the TEM instability, but may be caused by the temperature dependence in the gyro-Bohm scaling, which correlates to the temperature dependence in the collisionality. More discharges at high density and consequently high collisionality are needed to further trace the observed ν^* trend.

Figure 11 shows a plot of $\chi_{\mathrm{eff}}/\chi_{\mathrm{gB}}$ over the localized plasma β at $r_{\mathrm{eff}} = 0.25$ m.

Low β yields a broad vertical spread of data points, while turbulent transport for the highest β values close to 2% is consistently reduced. This can be interpreted as the beneficial β

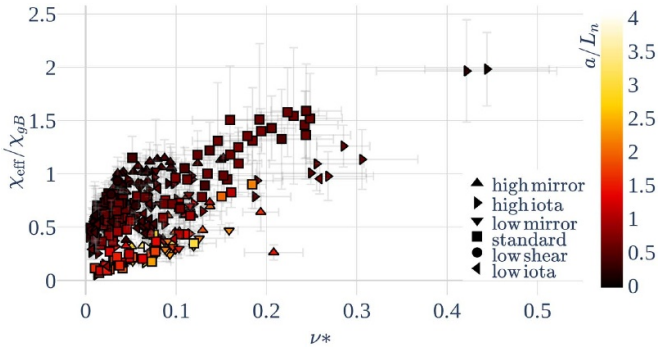

Figure 10. Scatterplot of gyro-Bohm normalized effective turbulent transport coefficient $\chi_{\mathrm{eff}}/\chi_{\mathrm{gB}}$ over normalized collisionality ν^*, a/Ln as color-scale. Error bars represent uncertainties of $\pm 3\,\sigma$, $r_{\mathrm{eff}} = 0.25$ m.

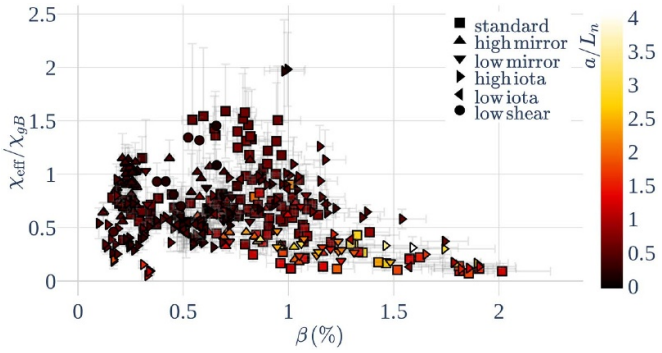

Figure 11. Scatterplot of gyro-Bohm normalized effective turbulent transport coefficient $\chi_{\mathrm{eff}}/\chi_{\mathrm{gB}}$ over localized plasma β, a/Ln as color-scale. Error bars represent uncertainties of $\pm 3\,\sigma$, $r_{\mathrm{eff}} = 0.25$ m.

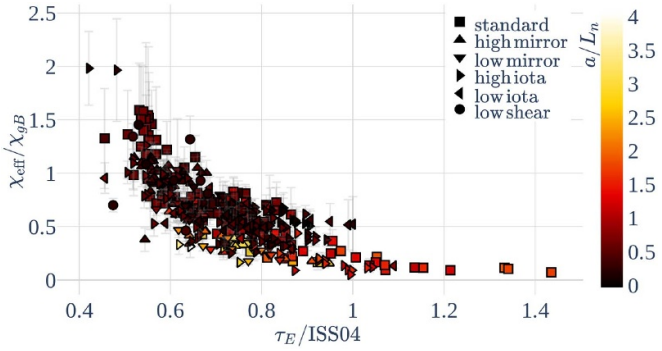

Figure 12. Scatterplots of gyro-Bohm normalized effective turbulent transport coefficient $\chi_{\mathrm{eff}}/\chi_{\mathrm{gB}}$ over global confinement time τ_E, normalized to ISS04, a/Ln as color-scale. Error bars represent uncertainties of $\pm 3\,\sigma$, $r_{\mathrm{eff}} = 0.25$ m.

stabilization effect on electrostatic modes. However, it must be noted that high β coincides with NBI and pellet fueled discharges and thereby ITG-suppressed scenarios. Likely, high β is only reached thanks to reduced turbulent transport in discharges in the database. In any case, the highest plasma pressure in the database is likely below the KBM threshold [24].

Figure 12 plots the normalized turbulent transport coefficient against the global confinement time τ_E, normalized to the ISS04 scaling [77]. In addition, the inversed density gradient length is included as a color-scale.

Global confinement time decays with turbulent transport, which is expected. All plasmas achieving a normalized confinement time over one, meaning higher than the ISS04 scaling, feature an increased density gradient. There is only minimal vertical scatter, which moreover suggests a universal physical behavior across heating and fueling schemes as well as magnetic configurations. $\tau_E/\mathrm{ISS04}$ was previously found to degrade with density at W7-X [78]. This effect is also present the database. However, turbulence suppressed scenarios featuring high density break this trend. Some discharges in low ι configuration appear shifted to the right from the central cloud of points, close to $\chi_{\mathrm{eff}}/\chi_{\mathrm{gB}} = 0.5$ and $\tau_E/\mathrm{ISS04} = 1$. This may be caused by the ι dependence in the ISS04 scaling, which might not accurately capture the behavior in W7-X.

Quantities used to calculate the confinement time are the diamagnetic energy, measured by diamagnetic loops [79] and the line integrated density, measured by interferometry [80]. Both of these are independent from the profile measurements used in the power balance analysis. Since figure 12 confirms the expected trend for turbulent transport, it serves as a cross-check for the plausibility of the power balance analysis presented in this study.

To further investigate the role of electron an ion turbulent transport, the reduced database with data points where the transport channels are separable is considered. Figure 13 shows $\chi_{\mathrm{e}}/\chi_{\mathrm{gB}}$ over a/L_n, figure 14 shows $\chi_{\mathrm{i}}/\chi_{\mathrm{gB}}$ over a/L_n. Data points are limited to those with $a/L_{T\mathrm{i}} > 1.5$ again.

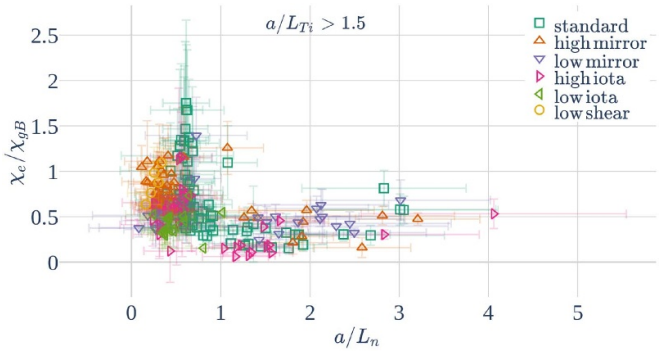

Figure 13. Scatterplot of gyro-Bohm normalized electron turbulent transport coefficient $\chi_{\mathrm{e}}/\chi_{\mathrm{gB}}$ over inverse density gradient length a/L_n, data points are limited to $a/L_{T\mathrm{i}} > 1.5$. Error bars represent uncertainties of $\pm 3\,\sigma$, $r_{\mathrm{eff}} = 0.25$ m.

In general, there is a clear turbulent transport reduction with density gradient in both channels. Above the value of about over $a/L_n = 1$, a baseline of about 0.5 gyro-Bohm units remains in the electron channel, with some scatter among the data points. Above $a/L_n = 2$, there a slight increase of electron channel turbulent transport, which is reminiscent of behavior seen nonlinear gyrokinetic simulations [12]. Turbulent transport in the ion channel is suppressed to nearly zero, with very little scatter across all magnetic configurations, heating and fueling schemes. Thus, turbulent transport in large density

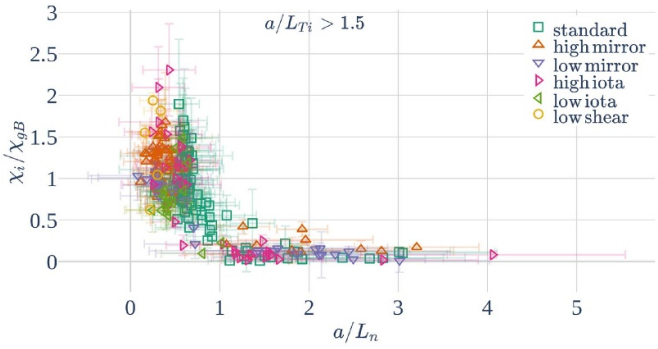

Figure 14. Scatterplot of gyro-Bohm normalized ion turbulent transport coefficient $\chi_\mathrm{i}/\chi_\mathrm{gB}$ over inverse density gradient length a/L_n, data points are limited to $a/L_{T\mathrm{i}} > 1.5$. Error bars represent uncertainties of $\pm 3\,\sigma$, $r_\mathrm{eff} = 0.25$ m.

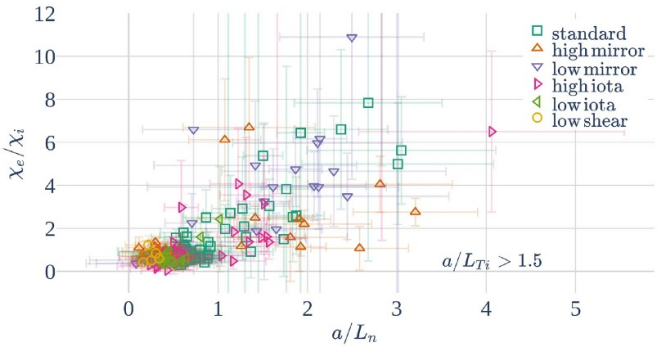

Figure 15. Scatterplot of electron- divided by ion turbulent transport coefficient $\chi_\mathrm{e}/\chi_\mathrm{i}$ over inverse density gradient length a/L_n, data points are limited to $a/L_{T\mathrm{i}} > 1.5$. Error bars represent uncertainties of $\pm 3\,\sigma$, $r_\mathrm{eff} = 0.25$ m.

gradient cases, as seen in figure 4(b), is determined mainly by the electron channel.

This behaviour is consistent with the dominant role of ITG modes at small a/L_n. ITG modes can drive turbulent transport in both channels, but they are completely stabilized by the density gradient. The identity of the turbulence driver for electron transport at $a/L_n > 1$ remains uncertain; ETG modes or temperature gradient driven TEMs could be responsible.

For additional visualization of the relation between the turbulent transport channels of electrons and ions, figure 15 depicts $\chi_\mathrm{e}/\chi_\mathrm{i}$ over a/L_n, $a/L_{T\mathrm{i}} > 1.5$.

5. Conclusion

In this paper, an extensive database of turbulent heat transport for a broad parameter range of plasma scenarios is presented. Dependencies of the turbulent transport on main physics parameters are studied. Plasma instabilities including ITG, ETG, TEM and KBM are introduced together with their observable driving parameters. The most important parameters for the turbulent transport coefficients are found to be the normalized gradients of density and ion temperature. A clear suppression of the turbulent transport with a/L_n is universally found in the database.

This suppression is most apparent in the ion channel of turbulent transport and less pronounced in the electron channel, such that the correlation is also reflected in the effective turbulent transport coefficient $\chi_\mathrm{eff}/\chi_\mathrm{gB}$. The normalized ion transport coefficient is roughly inversely proportional to a/L_n for small density gradients and is nearly zero for $a/L_n > 1$. This behaviour can be interpreted as either a continuous dependency or a critical transition between two transport regimes at $a/L_n = 1$.

In contrast, the normalized electron transport coefficients remains at approximately 0.5 gyro-Bohm units for $a/L_n > 1$. This residual electron transport can be due to ETG modes or temperature gradient driven TEMs. With the experimental methods at hand, the underlying instability cannot be decided.

A critical parameter of $a/L_n = 1$ is in agreement with findings in other works regarding W7-X. NBI heated discharges show a change of turbulent particle transport at $a/L_n = 1.1$ [49]. Out of a set of discharges with ECRH and NBI heating, those with $a/L_n > 1$ at $r_\mathrm{eff}/a = 0.4$ exhibit a reduction in turbulent χ by a factor of 4 [26]. Turbulent impurity transport changes with a critical parameter of $a/L_n = 1$, central peaking of impurity density is absent up to $a/L_n = 1$ and increases for larger values [81]. In simulations with the gyrokinetic code stella, a decrease of mode growth between $a/L_n = 1.25 - 2.75$ and a strong reduction of the ion heat flux with increasing density gradients is found [12].

Since turbulence suppression with density gradient length is present and equivalent across all heating and fueling schemes in the database, the effect appears to be fundamental to plasma physics, rather than being an artifact of machine operation.

In addition, a trend to larger turbulent transport coefficients with increasing $a/L_{T\mathrm{i}}$ exists, although with no clear turbulence suppression as with a/L_n. Discharges with off-axis heating may weaken the $a/L_{T\mathrm{i}}$ trend. Doppler reflectometry yields similar trends of the density fluctuation amplitude with $a/L_{T\mathrm{i}}$ and a/L_n [19].

These experimental findings are in agreement with theoretical predictions for ITG modes. This study demonstrates the effectiveness of NBI and pellet injection for turbulence suppression via density gradient peaking.

Selected plasma scenarios from the database with suppressed turbulence are discussed in detail. An example discharge showcases the reduced turbulence following pellet injection.

A discharge at low power ECR heating following a boronization of the first wall shows strongly reduced turbulent transport. This can be attributed to spontaneous density gradient formation following reduced hydrogen outgassing from the first wall.

The temperature ratio $T_\mathrm{e}/T_\mathrm{i}$ does not strongly exacerbate transport in the database. While such an effect is theoretically expected, it may be masked by stronger parameter dependencies like that with the temperature gradient. Experiments with well controlled profile gradients would be necessary to measure the $T_\mathrm{e}/T_\mathrm{i}$ exacerbation.

The ETG length is uncorrelated to turbulent transport in the ITG dominated regime, which lends no direct evidence for the influence of ETG modes.

There is a positive trend of $\chi_{\mathrm{eff}}/\chi_{\mathrm{gB}}$ with the normalized collisionality ν^*, which may be a result of the temperature dependence in the gyro-Bohm scaling. More experiments at high electron density and collisionality are needed to trace this trend. Non-normalized turbulent transport is largely uncorrelated to normalized collisionality in the database. Turbulent transport being unaffected by collisionality is found in previous experimental studies and is not contradicting the presence of TEMs [20].

A plot of $\chi_{\mathrm{eff}}/\chi_{\mathrm{gB}}$ over the local plasma β at mid radius shows a broadly scattered distribution, which allows no direct conclusion on the presence of KBMs. In the considered parameter range, the dominant turbulent transport is likely due to electrostatic instabilities. There appears to be a slight reduction in the vertical spread of data points at high β, which coincides with ITG suppressed scenarios. However, the highest β close to 2% might still be too low to destabilize KBMs [24], a boundary which might be pushed further in future experiments.

Global confinement time normalized to ISS04 [77] is calculated independently from the power balance analysis, using diamagnetic loops [79] and interferometry [80]. As expected, the global confinement time decays with increasing turbulent transport coefficients in the database. There is only minimal vertical scatter, which serves as a cross-check for the power balance analysis. All plasmas achieving a normalized confinement time over one feature an increased density gradient.

Turbulent transport found in the database typically exceeds neoclassical transport by more than a factor of 10, except for turbulence suppressed scenarios.

No clear difference in transport characteristic between the standard, low mirror and high ι configurations can be extracted from the database. Configuration dependencies are overlaid by the uncertainties of the plasma profiles, which have a greater effect on turbulent transport. It appears that the turbulence suppression is less effective in the high mirror configuration, compared to the other configurations. A strong reduction in turbulent is only reached above $a/L_n = 2$. For the low ι and low shear configurations, the sample size of discharges with turbulence suppression is too small to draw a final conclusion.

In intermediate high ι, limiter configurations found to have improved global confinement time, one would expect a significant alteration of turbulent transport [27]. This is probably linked to a transport barrier localized at the internal islands, with no visible effect around mid radius. A future publication may be dedicated to resolving turbulent transport in such high ι plasmas.

Lastly, the presented database contains discharges from 2018 to 2025, corresponding to the operation phases OP1.2b, OP2.1., OP2.2. and OP2.3. Further experiments including higher β values as well as helium-fueled plasmas may be explored in future publications.

Data availability statement

The data cannot be made publicly available upon publication because no suitable repository exists for hosting data in this field of study. The data that support the findings of this study are available upon reasonable request from the authors.

Acknowledgment

The authors would like to thank J H E Proll and D Carralero for useful comments and discussion.

This work has been carried out within the framework of the EUROfusion Consortium, funded by the European Union via the Euratom Research and Training Programme (Grant Agreement No 101052200 - EUROfusion). Views and opinions expressed are however those of the author(s) only and do not necessarily reflect those of the European Union or the European Commission. Neither the European Union nor the European Commission can be held responsible for them.

Conflict of interest

The authors have no conflicts to disclose.

Author Contributions

M. Wappl: Methodology (equal); Software (equal); Formal analysis (lead); Investigation (lead); Writing—original draft (lead); Visualization (lead). **S.A. Bozhenkov**: Conceptualization (lead); Methodology (equal); Software (equal); Validation (lead); Writing—review & editing (lead); Supervision (equal). **T. Andreeva**: Investigation (equal); Resources (equal). **S. Bannmann**: Software (equal); Resources (equal). **H.M. Smith**: Software (equal); Resources (equal); Writing—review & editing (equal). **R.C. Wolf**: Supervision (lead).

References

[1] Beidler C *et al* 2021 *Nature* **596** 221
[2] Wesson J 2011 *Tokamaks; 4th ed* (*International Series of Monographs on Physics*) (Oxford University Press)
[3] Dinklage A, Klinger T, Marx G and Schweikhard L 2005 *Plasma Physics* (Springer)
[4] Scott B 2021 *Turbulence and Instabilities in Magnetised Plasmas* vol 2 (IOP Publishing) pp 2053–563
[5] Proll J H E 2014 Trapped-Particle Instabilities in Quasi-Isodynamic Stellarators *PhD Thesis* Ernst-Moritz-Arndt-Universität Greifswald (available at: https://epub.ub.uni-greifswald.de/frontdoor/index/index/year/2014/docId/1264/)
[6] Beurskens M *et al* 2021 *Nucl. Fusion* **61** 116072
[7] Riemann J, Kleiber R and Borchardt M 2016 *Plasma Phys. Control. Fusion* **58** 074001
[8] Xanthopoulos P *et al* 2020 *Phys. Rev. Lett.* **125** 075001

[9] Kuczyński M *et al* (the W7-X Team) 2024 *Nucl. Fusion* **65** 016019
[10] Manfredi G and Ottaviani M 1997 *Phys. Rev. Lett.* **79** 4190
[11] Xanthopoulos P, Merz F, Görler T and Jenko F 2007 *Phys. Rev. Lett.* **99** 035002
[12] Thienpondt H, García-Regaña J, Calvo I, Acton G and Barnes M 2024 *Nucl. Fusion* **65** 016062
[13] Bañón Navarro A, Di Siena A, Velasco J, Wilms F, Merlo G, Windisch T, LoDestro L, Parker J and Jenko F 2023 *Nucl. Fusion* **63** 054003
[14] Jenko F, Dorland W, Kotschenreuther M and Rogers B N 2000 *Phys. Plasmas* **7** 1904
[15] Zocco A, Podavini L, Wilms F, Bañón Navarro A and Jenko F 2024 *Phys. Rev. Res.* **6** 033099
[16] Krämer-Flecken A *et al* (the W7-X-team) 2025 *Plasma Phys. Control. Fusion* **67** 025014
[17] Gerard M, Geiger B, Pueschel M, Bader A, Schmitt J and Kumar S 2020 *62nd Annual Meeting of the APS Division of Plasma Physics* (available at: https://hsx.wisc.edu/wp-content/uploads/sites/747/2022/10/APS_Poster_11-2020MichaelJeffreyGerard.pdf/)
[18] Morren M C L, Proll J H E, van Dijk J and Pueschel M J 2024 *Phys. Plasmas* **31** 052508
[19] Carralero D *et al* 2021 *Nucl. Fusion* **61** 096015
[20] Carralero D *et al* 2022 *Plasma Phys. Control. Fusion* **64** 044006
[21] Beidler C *et al* 2011 *Nucl. Fusion* **51** 076001
[22] Scott B 2021 *Turbulence and Instabilities in Magnetised Plasmas* vol 1 (IOP Publishing) pp 2053–563
[23] Aleynikova K and Zocco A 2017 *Phys. Plasmas* **24** 092106
[24] Aleynikova K, Zocco A, Xanthopoulos P, Helander P and Nührenberg C 2018 *J. Plasma Phys.* **84** 745840602
[25] Miyamoto K 2016 *Plasma Physics for Controlled Fusion* (Springer)
[26] Ford O *et al* (the W7-X Team) 2024 *Nucl. Fusion* **64** 086067
[27] Andreeva T *et al* (the W7-X Team) 2022 *Nucl. Fusion* **62** 026032
[28] Bozhenkov S *et al* 2020 *Nucl. Fusion* **60** 066011
[29] Warmer F *et al* 2021 *Phys. Rev. Lett.* **127** 225001
[30] Lu X X *et al* 2017 *44th EPS Conf. on Plasma Physics*
[31] Kin F *et al* 2023 *Phys. Plasmas* **30** 112505
[32] Wang C *et al* 2024 *Plasma Phys. Control. Fusion* **66** 022001
[33] Swee C, Geiger B, Dux R, Kumar S T A, Castillo J F, Bader A and Gerard M 2021 *Plasma Phys. Control. Fusion* **64** 015008
[34] Leonard A, Lasnier C, Cuthbertson J, Evans T, Fenstermacher M, Hill D, Jong R, Meyer W, Petrie T and Porter G 1995 *J. Nucl. Mater.* **220–222** 325
[35] Callahan K *et al* 2023 *Nucl. Fusion* **63** 126009
[36] Citrin J *et al* 2014 *Plasma Phys. Control. Fusion* **57** 014032
[37] Matthews G F *et al* 2017 *Phys. Scr.* **2017** 014035
[38] Doerk H, Bock A, Di Siena A, Fable E, Görler T, Jenko F, Stober J and Team T A U 2017 *Nucl. Fusion* **58** 016044
[39] Molina Cabrera P A *et al* 2023 *Phys. Plasmas* **30** 082304
[40] Liu J *et al* (the EAST Team) 2022 *Nucl. Fusion* **63** 016011
[41] Budny R 2005 *IAEA Conf. on H-Mode and Internal Barrier Physics*
[42] Shirai H, Hirayama T, Shimizu K, Takizuka T and Azumi M 1989 *Nucl. Fusion* **29** 805
[43] Lee Y *et al* 2023 *Nucl. Fusion* **63** 126032
[44] Weir G *et al* (the W7-X Team) 2021 *Nucl. Fusion* **61** 056001
[45] Ida K *et al* (the LHD experimental group) 2005 *32nd European Physical Society Conf. on Plasma Physics and Controlled Fusion Combined With the 8th Int. Workshop on Fast Ignition of Fusion Targets (Tarragona, Spain)*
[46] Geiger B, Ford O, Beurskens M, Weir G, Lazerson S, Bozhenkov S, Faber B, Simko S and Poloskei P (the W7-X Team) 2022 *64th Annual Meeting of the APS Division of Plasma Physics*
[47] Simko S, Swee C, Ford O, Romba T, Lazerson S and Geiger B (the W7-X Team) 2023 *65th Annual Meeting of the APS Division of Plasma Physics*
[48] Huang Z, Edlund E, Porkolab M, Bähner J-P, Böttger L-G, Sehren C V, Stechow A V and Grulke O 2021 *J. Instrum.* **16** 01014
[49] Bannmann S *et al* (the W7-X Team) 2024 *Nucl. Fusion* **64** 106015
[50] Romba T, Reimold F, Jaspers R, Ford O, Vanó L and Klinger T (the W7-X Team) 2023 *Nucl. Fusion* **63** 076023
[51] Wegner T *et al* 2018 *Rev. Sci. Instrum.* **89** 073505
[52] Wegner T, Bähner J-P, Buttenschön B, Langenberg A and von Stechow A 2023 *J. Plasma Phys.* **89** 955890302
[53] Pasch E *et al* 2016 *Rev. Sci Instrum.* **87** 11E729
[54] Bozhenkov S *et al* 2017 *J. Instrum.* **12** 10004
[55] Fuchert G *et al* 2022 *J. Instrum.* **17** C03012
[56] Pablant N A *et al* 2012 *Rev. Sci. Instrum.* **83** 083506
[57] Pablant N A *et al* 2014 *Rev. Sci. Instrum.* **85** 11E424
[58] Wappl M *et al* 2024 *Rev. Sci. Instrum.* **95** 093529
[59] Ford O P *et al* 2024 *Rev. Sci. Instrum.* **95** 083526
[60] Ford O P *et al* 2020 *Rev. Sci. Instrum.* **91** 023507
[61] Kirov K K *et al* 2002 *Plasma Phys. Control. Fusion* **44** 2583
[62] Ott W, Speth E and Stäbler A 1977 Slowing-down of fast ions in a plasma: energy transfer, charge exchange losses and wall sputtering *Technical Report* Max-Planck-Institut für Plasmaphysik (available at: https://hdl.handle.net/11858/00-001M-0000-0027-6C43-5/)
[63] Lazerson S A *et al* 2020 *Nucl. Fusion* **60** 076020
[64] Gao J *et al* 2014 *Rev. Sci. Instrum.* **85** 043505
[65] Zhang D *et al* 2021 *Nucl. Fusion* **61** 116043
[66] Hirshman S P *et al* 1986 *Phys. Fluids* **29** 2951
[67] Turkin Y *et al* 2011 *Phys. Plasmas* **18** 022505
[68] Smith H 2022 Neotransp (available at: https://gitlab.mpcdf.mpg.de/smithh/neotransp/)
[69] van Rij W I and Hirshman S P 1989 *Phys. Fluids B* **1** 563
[70] Pablant N A *et al* 2018 *Phys. Plasmas* **25** 022508
[71] Alonso J *et al* (the W7-X Team) 2022 *Nucl. Fusion* **62** 106005
[72] Kuczyński M *et al* 2024 *Nucl. Fusion* **64** 046023
[73] Kleiber R *et al* 2024 *Comput. Phys. Commun.* **295** 109013
[74] Estrada T *et al* 2021 *Nucl. Fusion* **61** 046008
[75] McCarthy K *et al* 2024 *Nucl. Fusion* **64** 066019
[76] Sánchez J *et al* 2011 *Nucl. Fusion* **51** 094022
[77] Dinklage A *et al* 2007 *Fusion Sci. Technol.* **51** 1–7
[78] Fuchert G *et al* 2020 *Nucl. Fusion* **60** 036020
[79] Rahbarnia K *et al* 2018 *Nucl. Fusion* **58** 096010
[80] Kornejew P, Triminio H, Heinrich S and Hirsch M 2013 *40th EPS Conf. on Plasma Physics*
[81] Romba T, Reimold F, Bannmann S, Bleher T, Ford O P, Poloskei P Z and Wappl M (the W7-X Team) 2025 *Plasma Phys. Control. Fusion* **67** 065016